Sound & Vibration 2026, 60(6), 4833.
https://doi.org/10.59400/sv4833

Article

Vibro-electrical performance of nickel-clustered monocrystalline-silicon photovoltaic cells: A data-informed analytical modal study

Elyor Saitov[1,*], Nurullo Zikrillaev[2], Abdusalom Umarov[1,3], Khayrulla Zikrillaev[2], Sayfillo Nasriddinov[4], Khikmat Makhmudov[2,5], Nigora Usmanova[2]

[1] University of Tashkent for Applied Sciences, 1 Gavkhar Street, Chilanzar District, Tashkent 100149, Uzbekistan
[2] Tashkent State Technical University named after Islam Karimov, University Street 2, Tashkent 100095, Uzbekistan
[3] Tashkent State Transport University, 1 Temiryulchilar Street, Tashkent 100167, Uzbekistan
[4] Tashkent regional branch of Astrakhan State Technical University. Tashkent region.100164, Republic of Uzbekistan
[5] Uzbek National Institute of Metrology, Farobiy Street, 333A, 333B, Tashkent 100174, Uzbekistan
*** Corresponding author:** Elyor Saitov, elyor.saitov@utas.uz

CITATION

Saitov E, Zikrillaev N, Umarov A, et. al. Vibro-electrical performance of nickel-clustered monocrystalline-silicon photovoltaic cells: A data-informed analytical modal study. Sound & Vibration. 2026r; 60(6): 4833. https://doi.org/10.59400/sv4833

COPYRIGHT

Copyright © 2026r by author(s). *Sound & Vibration* is published by Academic Publishing Pte Ltd. This work is licensed under the Creative Commons Attribution (CC BY) license. https://creativecommons.org/licenses/by/4.0/

Abstract: Dynamic mechanical loading can initiate cracks, interconnect damage, and power loss in crystalline-silicon photovoltaic assemblies, yet the local vibration consequences of metallic impurity clusters inside a cell remain poorly quantified. This study combines previously published electrical and microstructural measurements for nickel-clustered monocrystalline-silicon cells [7] with a reproducible plate-vibration model. The records cover 600-1100 °C additional annealing, reported cluster-size intervals of 1-30 μm, open-circuit voltages of 480-506 mV, and short-circuit current densities of 20.2-45.7 mA cm^{-2}. A 10 × 5 × 0.38 mm coupon was represented as a simply supported Kirchhoff-Love plate, with the unreported crystal orientation bracketed by silicon Young's moduli of 130-169 GPa. An independent Mindlin-Reissner eigenvalue calculation, including transverse shear and rotary inertia, predicted a first frequency 1.26% below the Kirchhoff-Love value. Pure-Ni inclusions and Reuss-Voigt stiffness bounds were retained as a conservative homogenization envelope. The Kirchhoff-Love first local bending frequency was 67.05-76.45 kHz. For the 900 °C condition with the highest UocJsc proxy calculated from the published data, the proxy was 2.190 times the control value, while the model predicted a first-mode shift of -0.0037% to -0.0040% for the midpoint morphology and -0.0006% to -0.0127% across its stated lower-upper morphology bounds. The maximum predicted reduction over the full feasible morphology domain was 3.051%. These calculations predict a small coupon-level modal effect under the stated geometry, support, and homogenization assumptions; they do not constitute experimental evidence of modal performance, fatigue resistance, or module-level vibration reliability.

Keywords: modal analysis; plate vibration; photovoltaic cells; Mindlin-Reissner plate theory; inclusion homogenization; harmonic response; thermal annealing

1. Introduction

Photovoltaic (PV) cells and modules encounter wind, transportation vibration, installation loads, and cyclic pressure during service. IEC TS 62782 formalizes cyclic dynamic mechanical loading of modules because solar cells, interconnect ribbons, electrical bonds, and edge seals can be damaged even when immediate power loss is not evident [1]. Mechanical-load experiments have shown that crack position and orientation affect the electrically separated area of crystalline-silicon cells [2]. For vehicle-integrated PV, experimental modal analysis has further demonstrated that

low-frequency modes and amplification depend strongly on module architecture, while the influence of the cell string differs between conventional glass modules and lightweight composite designs [3]. Analytical homogenization and plate theory can therefore provide useful early-stage estimates before a complete finite-element or experimental campaign [4].

Nickel (Ni) doping offers a different route to altering PV performance. Nickel is a very fast interstitial diffuser in silicon and can precipitate readily during cooling; the precipitates may be recombination-active, so temperature history and quenching are decisive [5]. Conversely, controlled cluster formation has been investigated as a means of creating distributed microbarriers, extending spectral response, and gettering unwanted impurities. Earlier work involving the present research line reported controllable Ni-cluster formation throughout silicon [6] and infrared sensitivity extending to approximately 4 μm in Ni-clustered silicon cells [7]. Subsequent studies identified processing windows in which Ni diffusion and annealing improved photoelectric response [8,9]. These electrical and microstructural findings do not, however, establish whether the additional dense inclusions measurably alter the local vibration characteristics of the brittle silicon coupon.

The present study addresses that missing link without presenting previously published electrical or microstructural findings as new experiments. The annealing temperatures, feature-size intervals, Uoc values, and Jsc values in **Table 1** were previously published in **Table 2** of reference [7]. References [6,8,9] provide additional context on Ni-cluster formation, composition, and processing. The UocJsc and relative-proxy columns, analytical vibration model, and independent Mindlin-Reissner model check are original to the present reanalysis. The objectives are to: (i) establish an orientation-aware baseline for the coupon's local bending modes; (ii) quantify the effect of transverse shear and rotary inertia on the first mode; (iii) estimate conservative Reuss-Voigt bounds for the frequency shift caused by the reported morphologies; (iv) compare the predicted mechanical shift with the electrical-response proxy calculated from the published measurements; and (v) define a reproducible harmonic-response envelope for future tests. The hypothesis is that the condition with the highest calculated UocJsc proxy produces a much smaller model-predicted change in local modal frequency than in the electrical proxy.

2. Materials and methods

2.1. Archival photovoltaic-cell dataset

The supplied records describe monocrystalline-silicon cells fabricated by diffusion-based junction formation and subsequent Ni incorporation. The annealing temperature, reported feature interval, Uoc, and Jsc values for all **Table 1** rows, including the undoped control, were previously published in **Table 2** of reference [7]. The present study calculates the UocJsc and relative-proxy columns from those published measurements and does not present the source measurements as new experiments. References [6,8,9] provide complementary processing and microstructural context. The specimens used for the electrical table were identified as n-type silicon, and the finished coupons were rectangular, 10 mm long, 5 mm wide, and approximately 380 μm thick. Different specimen groups in the published source used different terminal hold times; because the present model does not infer diffusion kinetics from those times, only the explicitly paired annealing temperature, feature-size interval, open-circuit voltage, and short-circuit current density were used.

Cluster morphology was observed using infrared microscopy after removal and

polishing of a near-surface layer. The records report approximately 10^5 cm^{-2} for 0.5–1.5 µm features and (5–6) × 10^4 cm^{-2} for 1–3 µm features. A broader temperature-specific table reports intervals up to 30 µm at 600–700 °C. **Figure 1** reproduces the supplied qualitative micrographs. Because the images contain no embedded scale bars, no dimensions were extracted from pixels; all dimensions used below come from the written records. The apparent absence of resolved features at 1200 °C is therefore interpreted only as being below the instrument's resolution, not as proof that clusters were absent.

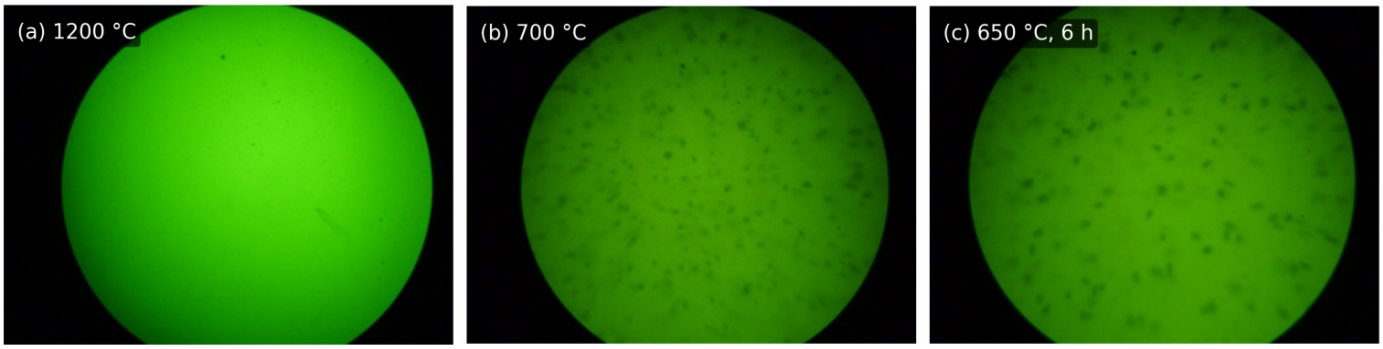


Figure 1. Archival infrared micrographs of the silicon specimens: (a) after high-temperature processing at 1200 °C, with no resolved features; (b) after additional annealing at 700 °C; (c) after annealing at 650 °C for 6 h. The images are qualitative because the supplied files contain no scale bars.

Table 1 reproduces the source measurements reported in reference [7, **Table 2**] and adds two derived columns calculated in the present study: UocJsc proxy and relative proxy. The control was described as not intentionally doped with Ni. The 0.5-1 µm morphological feature reported in the control row of the source record was not interpreted as a Ni cluster and was excluded from the mechanical homogenization.

Table 1. Previously published post-anneal morphology and measured electrical data from reference [7, **Table 2**], with UocJsc and relative-proxy columns calculated in the present study.

Additional anneal (°C)	Reported feature interval (µm)	Uoc (mV)	Jsc (mA cm^{-2})	UocJsc proxy (mW cm^{-2})	Relative proxy
600	2–30	500	20.4	10.200	0.981
700	2–30	503	20.2	10.161	0.978
800	2–20	506	28.1	14.219	1.368
900	2–5	498	45.7	22.759	2.190
1000	2–5	482	21.4	10.315	0.992
1100	1–2	480	20.9	10.032	0.965
Undoped control	not used in model	507	20.5	10.394	1.000

The product P* = UocJsc was retained because it is the only joint voltage-current quantity recoverable from every row of the published source table. For a photovoltaic cell measured at incident power density Pin, conversion efficiency satisfies $\eta = P_{max}/P_{in} = U_{oc}J_{sc}FF/P_{in}$, where FF is the fill factor. The published source contains neither complete current-voltage curves nor Pmax, FF, calibrated incident irradiance, a consistently documented active area, replicate-level observations, or confidence

intervals. Back-calculating efficiency would therefore require untestable assumptions and would create an unjustified appearance of precision. Reporting P* preserves the measured voltage and current-density information without presenting it as maximum power or efficiency.

The normalized value R* = (UocJsc)i/(UocJsc)control is interpreted only as a descriptive within-dataset ranking. That interpretation assumes common active area, illumination spectrum and irradiance, cell temperature, contact geometry, and acquisition protocol. Under those conditions, common scale factors do not change the ranking. The normalization neither assumes FF = 1 nor converts the product into efficiency.

Fill factor can change independently through series resistance, shunt leakage, recombination, junction quality, or contact degradation. Under otherwise common test conditions, the maximum-power ratio would be Pmax,900/Pmax,control = 2.190(FF900/FFcontrol). Thus, a 10%, 20%, or 50% lower FF at 900 °C would reduce the implied maximum-power ratio to 1.971, 1.752, or 1.095, respectively; a decrease greater than 54.3% would be required to remove the proxy advantage entirely. These scenarios illustrate sensitivity but do not estimate the missing FF. Accordingly, 900 °C is described only as the condition with the highest UocJsc proxy calculated from the published data, not as an electrically optimal or efficiency-maximizing condition. Controlled retesting must acquire complete current-voltage curves under calibrated irradiance and cell temperature.

2.2. Baseline thin-plate model

The isolated cell was idealized as a homogeneous, simply supported Kirchhoff-Love rectangular plate. This boundary condition provides an exact Navier solution and a reproducible local-coupon reference; it does not represent a laminated module or bonded cell. The thickness-to-short-side ratio is h/b = 0.076, motivating the independent shear-deformable model check described in Section 2.3. The flexural rigidity is:

$$D = Eh^3 / [12(1 - \nu^2)], \quad (1)$$

where E is Young's modulus, h is thickness, and ν is Poisson's ratio. The natural frequency of mode (m,n) is [4,10]

$$f_{mn} = (\pi/2) \sqrt{[D/(\rho h)]} [(m/a)^2 + (n/b)^2], \quad (2)$$

where a and b are the plate dimensions and ρ is mass density. Single-crystal silicon is anisotropic. Because the wafer orientation and in-plane cutting direction were not reported, E was bracketed from 130 to 169 GPa instead of assigning a false precision [11]. The baseline calculation used ρSi = 2329 kg m^{-3} and νSi = 0.28. This modulus interval is propagated into the reported modal-frequency range.

2.3. Independent Mindlin-Reissner model check

To test the thin-plate baseline independently, the first simply supported mode was recalculated with a first-order shear-deformation Mindlin-Reissner formulation [15]. The transverse displacement and two rotations were expanded with compatible trigonometric trial functions for the (1,1) mode. The resulting 3 × 3 generalized eigenproblem included transverse shear with correction factor κ = 5/6 and rotary inertia $\rho h^3/12$. The same geometry, density, Poisson's ratio, and Young's-modulus bracket used in the Kirchhoff-Love calculation were retained, so the comparison isolates shear-deformation and rotary-inertia effects. The Navier trial functions satisfy zero transverse displacement and normal bending moment, with zero tangential rotation, on each edge.

The generalized eigenproblem $Kq = \omega^2 Mq$ was solved in double precision. The comparison metric was 100(fMR - fKL)/fKL for each endpoint of the silicon-modulus bracket. An independently implemented energy-integral assembly and a scalar quadratic reduction were used as numerical consistency checks. This is a comparison between plate models, not experimental validation.

2.4. Conservative cluster homogenization

The written microscopy records provide projected number density rather than a three-dimensional size distribution or depth profile. Each observed feature was therefore represented as one equivalent spherical inclusion in a single projected layer through the coupon thickness. The single-layer construction is not a claim that precipitates occupy one physical plane; it is a volume-equivalence mapping that converts the reported two-dimensional count into an explicit, reproducible upper-bound mass estimate. It neglects clustering through depth, interface compliance, and local residual stress, which are retained as limitations. For diameter d and surface density NA, the equivalent volume fraction is:

$$\varphi = NA\pi d^3/(6h), \tag{3}$$

and projected area coverage is $\eta A = NA\pi d^2/4$. Parametric points with $\eta A > 0.50$ were excluded to avoid an overlapping-sphere interpretation. The conservative endpoint assigns every equivalent sphere the properties of pure Ni: $\rho Ni = 8908$ kg m^{-3}, $ENi = 200$ GPa, and $\nu Ni = 0.31$ [12]. Published microanalysis indicates that cluster composition depends on processing and location: approximately 60% Ni and 40% Si was reported in one bulk microprobe study [6], whereas another investigation reported primarily Si with up to about 15% Ni [9]. For a Ni-Si inclusion, both equivalent density and stiffness contrast decrease toward the Si matrix values. Composition sensitivity was therefore evaluated at Ni volume fractions of 0.15, 0.60, and 1.00 in the inclusion; the pure-Ni case produced the largest negative first-mode shift and is retained as the conservative bound. For each prescribed Ni volume fraction, inclusion stiffness was first mixed using nested Reuss and Voigt bounds; density and Poisson's ratio were mixed linearly. These are volume-fraction scenarios, not conversions of measured atomic or mass fractions. The elastic bounds were:

$$EV = (1 - \varphi)ESi + \varphi ENi, \tag{4}$$

$$ER = [(1 - \varphi)/ESi + \varphi/ENi]^{-1}, \tag{5}$$

where subscripts V and R denote Voigt and Reuss estimates. Bergmann et al. used a related bounding strategy for layered PV-module frequencies [4]. For the nominal temperature comparison, each reported size-interval midpoint and $NA = 5.5 \times 10^4$ cm^{-2} were used. Lower-bound cases combine the reported minimum diameter with $NA = 5.0 \times 10^4$ cm^{-2}, and upper-bound cases combine the maximum diameter with $NA = 6.0 \times 10^4$ cm^{-2}. A separate sweep covered 0.5-30 μm and $(5\text{-}10) \times 10^4$ cm^{-2} under the area-coverage restriction. The full feasible-domain maximum was checked on the exact coverage boundary rather than inferred from the plotted density slices.

2.5. Harmonic-response envelope

The first plate mode was reduced to a single-degree-of-freedom response under uniform base acceleration. With frequency ratio $r = f/f11$ and damping ratio ζ, normalized relative-displacement amplification is

$$H(r,\zeta) = [(1 - r^2)^2 + (2\zeta r)^2]^{-1/2}. \tag{6}$$

For the (1,1) sine mode, the participation factor under uniform base acceleration is $\Gamma = 16/\pi^2$. The exact-resonance modal amplitude under acceleration ab is qres =

Γab/(2ζω11²). A conservative surface bending strain was computed from the sum of principal modal curvatures:

$$\varepsilon res = (h/2)\pi^2(a^{-2} + b^{-2})qres. \quad (7)$$

Because damping was not measured, ζ = 0.005, 0.010, and 0.020 were treated as sensitivity values rather than fitted properties. Calculations used double-precision arithmetic, with standard gravity taken as 9.80665 m s⁻². The Kirchhoff-Love implementation was checked against thin-plate scaling and the exact Navier solution; the first-mode baseline was then compared with the independent Mindlin-Reissner eigenvalue calculation in Section 2.3.

3. Results

3.1. Published electrical response across annealing temperature

The highest UocJsc proxy calculated from the published measurements occurred after the 900 °C additional anneal (**Figure 2a**). The reported Jsc was 45.7 mA cm⁻², 2.23 times the control value, while Uoc was 1.8% lower than the control. Their product was 22.759 mW cm⁻², corresponding to a relative proxy of 2.190. The 800 °C condition ranked second at 1.368. Values at 600, 700, 1000, and 1100 °C were approximately 0.8-3.5% below the control proxy. Because the published dataset contains no replicates or confidence intervals, these values provide a descriptive ranking rather than evidence of a statistically established optimum.

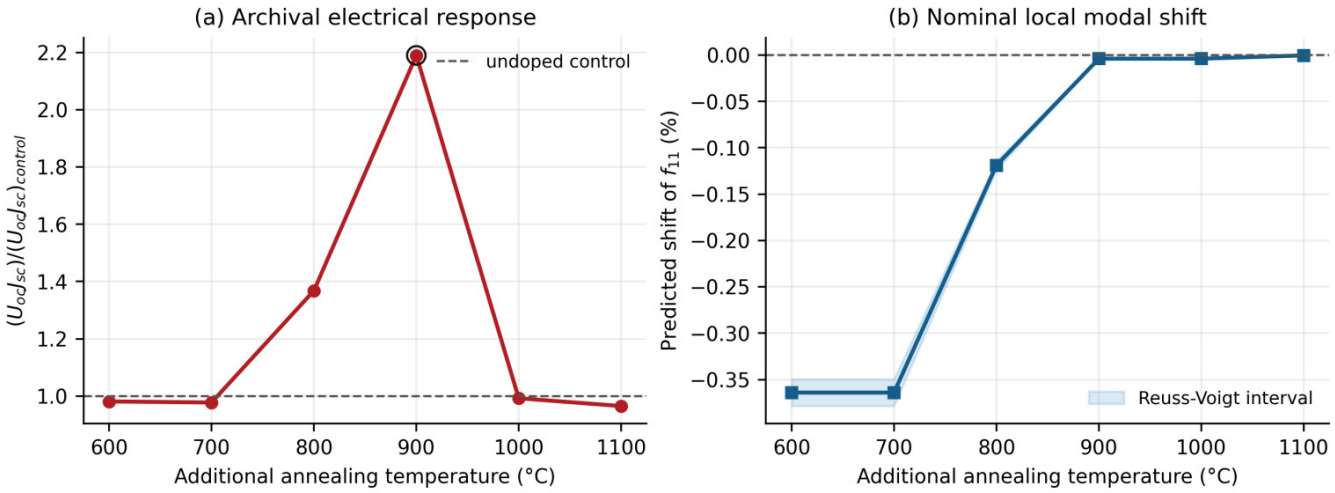


Figure 2. Coupled reanalysis across additional annealing temperature: (a) electrical-response proxy calculated from previously published measurements [7] and normalized by the undoped control; (b) analytically predicted first local-mode shift using each reported size-interval midpoint, a surface density of 5.5 × 10⁴ cm⁻², and Reuss-Voigt stiffness bounds.

The 900 °C condition with the highest calculated proxy should not be confused with the 800-850 °C Ni diffusion window reported elsewhere [8]. Diffusion temperature and subsequent morphology-setting anneal are different process variables. Modern diffusivity measurements also show that interstitial Ni transport is substantially faster than older estimates, reinforcing the need to control the complete thermal trajectory rather than interpret one temperature in isolation [5].

3.2. Baseline local modes

For ESi = 130 GPa, the analytically predicted Kirchhoff-Love frequencies of the first six selected local modes ranged from 67.05 to 496.17 kHz (**Table 2**). Increasing

ESi to 169 GPa raised f11 to 76.45 kHz and the highest listed frequency to 565.72 kHz. The independent Mindlin-Reissner eigenvalue solution gave f11 = 66.207 kHz at 130 GPa and 75.488 kHz at 169 GPa, 1.257% below the corresponding Kirchhoff-Love predictions at both endpoints. Thus, transverse shear and rotary inertia modestly lower the baseline but do not alter its frequency scale. The 14.0% crystallographic-modulus bracket remains much larger than either the 1.257% plate-theory difference or the nominal cluster-induced shift.

Table 2. Analytically predicted Kirchhoff-Love local-coupon frequencies.

Mode (m,n)	Frequency at E = 130 GPa (kHz)	Frequency at E = 169 GPa (kHz)
(1,1)	67.05	76.45
(2,1)	107.28	122.32
(3,1)	174.33	198.77
(1,2)	227.97	259.93
(2,2)	268.20	305.79
(1,3)	496.17	565.72

These are local modes of the millimetre-scale silicon coupon. They are not module modes: recent vehicle-integrated module tests found several assembly modes within 0–120 Hz [3]. The frequency-scale separation is expected because frames, glass or composite skins, encapsulants, adhesive interfaces, and large spans govern module dynamics.

3.3. Effect of cluster morphology on the first mode

For the 900 °C condition with the highest calculated proxy, the midpoint diameter is 3.5 μm. With NA = 5.5×10^4 cm^{-2}, Equation (3) gives φ = 0.00325% and ηA = 0.529%. The pure-Ni Reuss and Voigt models predict f11 shifts of -0.00399% and -0.00368%, respectively. Across the stated 2-5 μm interval and NA = (5-6) × 10^4 cm^{-2}, the full bound is -0.01269% to -0.00063% (**Table 3**). These are model predictions, not measured modal shifts.

Table 3. Analytically predicted lower, midpoint, and upper morphology bounds at ESi = 130 GPa.

Anneal (°C)	d range (μm)	φ range (%)	Area coverage range (%)	Midpoint shift (%)	Full bound shift (%)
600	2-30	0.000551-2.232	0.157-42.41	-0.379 to -0.350	-2.610 to -0.00063
700	2-30	0.000551-2.232	0.157-42.41	-0.379 to -0.350	-2.610 to -0.00063
800	2-20	0.000551-0.6614	0.157-18.85	-0.124 to -0.114	-0.800 to -0.00063
900	2-5	0.000551-0.01033	0.157-1.178	-0.00399 to -0.00368	-0.01269 to -0.00063
1000	2-5	0.000551-0.01033	0.157-1.178	-0.00399 to -0.00368	-0.01269 to -0.00063
1100	1-2	0.0000689-0.000661	0.0393-0.1885	-0.00031 to -0.00029	-0.00081 to -0.00008

Table 3 shows that the midpoint ordering is preserved, although the lower endpoints of overlapping reported diameter intervals are not distinguishable. The key inference is robust: even the upper 900 °C morphology bound predicts a first-

mode reduction of only 0.01269%. The full morphology sweep in **Figure 3** is cubic in diameter through Equation (3), so diameter has the greatest influence. For the full continuous domain under $\eta A \leq 50\%$, the maximum equivalent volume fraction is 2.63158% and the largest predicted frequency reduction is 3.05100%. This endpoint occurs at d = 30 μm and NA = 7.073553 × 10^4 cm^{-2}, where projected coverage is 50%; it is not the 900 °C condition.

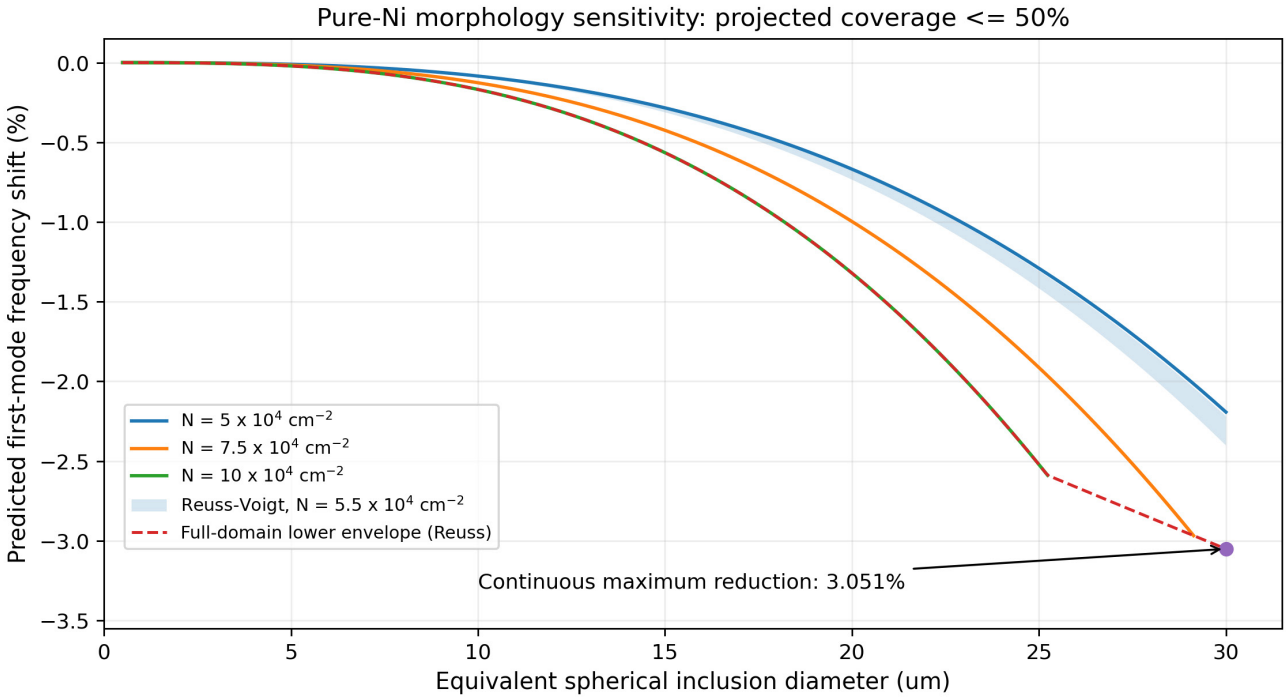


Figure 3. Recalculated first-mode sensitivity to equivalent cluster diameter and projected surface density. Solid curves show Reuss predictions at the labelled densities and terminate at 50% coverage; the shaded region is the Reuss-Voigt interval at 5.5 × 10^4 cm^{-2}. The dashed line is the lower envelope over the full permitted density interval, and the marked endpoint is its maximum predicted reduction.

A one-at-a-time sensitivity analysis about the 900 °C midpoint case confirms that the predicted shift is most sensitive to equivalent diameter because φ scales with d^3 (**Table 4**). Number density acts linearly, whereas the silicon modulus, inclusion modulus, and inclusion-density brackets have smaller absolute effects at this low volume fraction. The inclusion-density range from ρSi to ρNi also brackets the Ni-Si composition cases: 15%, 60%, and 100% Ni inclusions predict shifts of approximately -0.00055% to -0.00060%, -0.00221% to -0.00240%, and -0.00368% to -0.00399%, respectively.

Table 4. One-at-a-time sensitivity of the analytically predicted first-mode shift at the 900 °C midpoint morphology.

Parameter	Values examined	Predicted shift envelope (%)	Interpretation
Silicon modulus ESi	130-169 GPa	-0.00431 to -0.00368	Absolute baseline changes strongly; relative cluster shift changes little.
Inclusion modulus ENi	130-220 GPa	-0.00456 to -0.00343	Stiffness contrast is secondary at small φ.
Inclusion density ρinc	2329-8908 kg m^{-3}	-0.00399 to +0.00090	Pure Ni gives the largest negative mass effect.

Continuation Table:

Parameter	Values examined	Predicted shift envelope (%)	Interpretation
Equivalent diameter d	2-5 μm	-0.01163 to -0.00069	Dominant nominal-morphology variable through d^3.
Projected density NA	(5-6) × 10^4 cm^{-2}	-0.00435 to -0.00335	Approximately linear influence.

3.4. Harmonic response and strain envelope

At the natural-frequency ratio r = 1, the analytically predicted normalized response is H = 1/(2ζ), giving amplification factors of 100, 50, and 25 for ζ = 0.005, 0.010, and 0.020 (**Figure 4b**). Despite these factors, the high local resonance and small coupon dimensions limit the calculated absolute deformation. At 1g exact-resonance excitation, the predicted peak displacement is 2.24-8.96 nm and the conservative surface strain is 0.21-0.84 με. At 10g, the corresponding predicted strain is 2.10-8.40 με (**Table 5**).

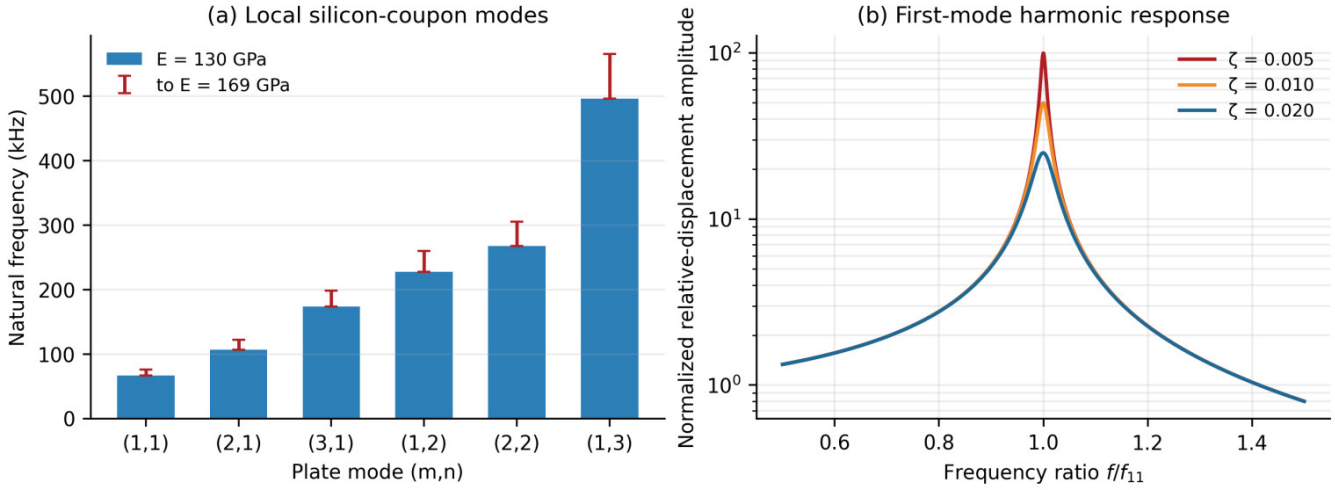


Figure 4. Analytical dynamic response of the undoped reference coupon: (a) selected local modal frequencies with the silicon modulus-orientation interval; (b) normalized first-mode harmonic response for three assumed damping ratios.

Table 5. Analytically predicted exact-resonance first-mode response at f11 = 67.05 kHz.

Damping ratio ζ	Base acceleration (g)	Peak q (nm)	Surface strain (με)	Biaxial stress estimate (MPa)
0.005	1	8.96	0.840	0.152
0.010	1	4.48	0.420	0.0758
0.020	1	2.24	0.210	0.0379
0.005	10	89.57	8.399	1.516
0.010	10	44.79	4.199	0.758
0.020	10	22.39	2.100	0.379

4. Discussion

4.1. Interpretation of electro-mechanical decoupling

The central model result is a separation between the electrical proxy calculated

from published measurements and predicted local dynamic sensitivity. At 900 °C, the calculated UocJsc proxy is 119% above the control value, while the midpoint inclusion model predicts a first-mode reduction of about four thousandths of one percent. Across the full 900 °C morphology bounds, the predicted reduction remains below 0.013%. This comparison is descriptive: the electrical published source reports no replicate-level uncertainty, and the vibration quantities are model outputs.

The predicted separation is mechanically plausible. At the 900 °C midpoint morphology, the equivalent inclusion volume fraction is only 3.25×10^{-5}. A pure-Ni sphere maximizes added density but also introduces a modest stiffness increase. When the inclusion is treated as a Ni-Si mixture, both properties move toward those of the matrix and the magnitude of the predicted negative shift decreases. The 15%, 60%, and 100% Ni composition cases give progressively larger negative shifts, confirming that the pure-Ni case is conservative for the present global-frequency metric. This conservatism does not extend to unknown local interface stresses or crack initiation.

The high calculated coupon frequencies do not imply that a complete PV product is immune to vibration. They imply that global module modes, mounting compliance, solder and ribbon fatigue, encapsulant viscoelasticity, and existing microcracks are likely to dominate the practical low-frequency response. This interpretation is consistent with module-scale studies [3,4,13] and with mechanical-load observations showing electrically consequential cracking [2]. The present chip-level model should therefore be nested inside, rather than substituted for, a full assembly model.

The comparison of uncertainty scales identifies what the model can resolve. Changing ESi from 130 to 169 GPa moves the Kirchhoff-Love f11 prediction by approximately 9.4 kHz. The Mindlin-Reissner result is 0.843-0.961 kHz lower than Kirchhoff-Love, whereas the nominal 900 °C pure-Ni state changes the 67.05 kHz prediction by only about 2.5-2.7 Hz. Consequently, any experimental cluster attribution requires controlled thickness, crystal orientation, temperature, support stiffness, residual stress, and remounting repeatability. Failure to resolve a few-hertz difference would be consistent with the model but would not validate its assumptions.

4.2. Proposed experimental validation protocol

A future validation program should use matched undoped controls and Ni-clustered coupons, prioritizing the 900 °C condition and optionally the larger-volume-fraction 600-700 °C cases. Wafer orientation, cutting direction, dimensions, metallization, contacts, specimen temperature, and mounting should be controlled; measurement order should be randomized and the replicate count set from a pilot repeatability study. A scanning laser Doppler vibrometer with low-amplitude shaker excitation and a fixture-reference accelerometer could provide frequency-response functions, fitted frequency and damping, and mode shapes for comparison by the modal assurance criterion [3,14]. Because the nominal predicted difference is only 2.5-2.7 Hz near 67 kHz, spectral resolution, temperature drift, and remounting variability must be below the target effect; otherwise a detection limit should be reported.

A second level should compare identically encapsulated control and treated mini-modules under low-frequency modal testing and cyclic dynamic mechanical loading [1]. Full current-voltage curves under calibrated irradiance and controlled cell temperature should accompany electroluminescence, thermography, and crack inspection so that FF, Pmax, efficiency, and uncertainty can be measured directly. Agreement would require the control frequency and mode shape to fall within specimen-specific predictions and the paired treated-control difference to

be repeatable. A larger or opposite shift would indicate contributions from support compliance, anisotropy, residual stress, nonuniform precipitation, or contact layers rather than invalidating the published electrical observations.

4.3. Limitations and domain of applicability

First, all vibration quantities reported here are analytical or numerical model predictions; the published source dataset contains no measured modal frequencies, mode shapes, damping ratios, or dynamic strains. The simply supported Kirchhoff-Love and Mindlin-Reissner calculations provide reproducible local-coupon baselines, not guaranteed resonances of fabricated devices. Real clamps, adhesives, encapsulants, and fixtures can alter both frequency and damping. Relative treated-control shifts are transferable only when geometry, temperature, and mounting are controlled.

Second, the homogenization maps a two-dimensional projected number density to a single layer of equivalent spherical inclusions. It does not resolve the true depth distribution, composition, interface condition, or precipitation-induced residual stress. The composition analysis shows that a Ni-Si inclusion produces a smaller global-frequency penalty than pure Ni, but Reuss-Voigt bounds apply only to the chosen mixture model and do not bound every spatial arrangement or local stress field. The 50% projected-coverage screen is a geometric rule, not a measured upper morphology.

Third, the isotropic plate models are first-order representations of an anisotropic processed semiconductor. The scalar modulus interval captures leading orientation uncertainty but not the full stiffness tensor. At $h/b = 0.076$, the Mindlin-Reissner calculation lowers f_{11} by 1.257%, showing a modest but nonzero shear and rotary-inertia effect. Metallization, junction layers, texture, thermal stress, cracks, geometric nonlinearity, and fatigue remain outside both models.

Fourth, the electrical comparison is descriptive rather than statistical. The annealing temperature, feature-size, Uoc, and Jsc values in Table 1 were previously published in reference [7], whereas UocJsc and relative proxy are calculated here. The published source provides no replicate-level values, sample counts, uncertainty estimates, complete current-voltage curves, or fill factors. The 2.190 UocJsc ratio cannot be assigned a confidence interval or converted into efficiency. An unknown FF change could strengthen or weaken the maximum-power ranking, as quantified in Section 2.1.

Taken together, these limitations restrict the conclusion to intact, linearly elastic coupons with the stated dimensions, support idealization, and morphology bounds. The model predicts that distributed cluster mass and mixture-law stiffness cause a small first-mode change at the 900 °C proxy maximum. It does not establish module vibration immunity, fatigue life, damage tolerance, or photovoltaic conversion efficiency.

5. Conclusion

A reproducible analytical extension and independent Mindlin-Reissner check place previously published Ni-clustered silicon-cell measurements [7] within a sound-and-vibration framework. For the 900 °C condition with the highest UocJsc proxy calculated in the present study, the ratio is 2.190 relative to the control. The pure-Ni midpoint model predicts a local first-mode shift of -0.0037% to -0.0040%, and the full 900 °C morphology bounds predict -0.0006% to -0.0127%. The Mindlin-Reissner baseline is 1.257% below the Kirchhoff-Love value, confirming that plate-theory

choice affects the absolute baseline more than the nominal cluster perturbation.

Within the stated geometry, simply supported boundary, and homogenization framework, the model therefore predicts that Ni-cluster mass and mixture-law stiffness have a small effect on the coupon's first local frequency. This is a model prediction, not an experimental finding, and it does not demonstrate an efficiency improvement, fatigue resistance, absence of local stress concentration, or module-level vibration reliability. The decisive next step is paired laser-vibrometry and shaker testing together with complete current-voltage characterization of control and treated specimens under identical conditions.

Author contributions: Conceptualization, E.S. and N.Z.; methodology, E.S. and K.Z.; validation, N.Z., A.U. and K.Z.; formal analysis, E.S. and K.Z.; investigation, N.Z.; resources, A.U. and K.Z.; data curation, E.S., N.Z. and K.M.; writing—original draft preparation, E.S. and S.N.; writing—review and editing, E.S., N.Z., A.U., K.Z., S.N., K.M. and N.U.; visualization, E.S., K.Z., S.N. and N.U.; supervision, A.U.; project administration, E.S., A.U., S.N. and N.U. All authors have read and agreed to the published version of the manuscript.

Funding: None.

Acknowledgment: None.

Conflict of interest: The authors declare no conflict of interest.

Data availability: All numerical inputs used in the analytical reanalysis are reported in Sections 2.1-2.5 and Tables 1-5. The annealing temperature, feature-size interval, Uoc, and Jsc values reproduced in Table 1 were previously published in reference [7, Table 2]. The UocJsc and relative-proxy columns and all vibration-model outputs are calculated in the present study. No new experimental dataset was generated for this analytical reanalysis.

References

[1] International Electrotechnical Commission. IEC TS 62782:2016: Photovoltaic (PV) Modules—Cyclic (Dynamic) Mechanical Load Testing. International Electrotechnical Commission; 2016.

[2] Kajari-Schröder S, Kunze I, Eitner U, Köntges M. Spatial and orientational distribution of cracks in crystalline photovoltaic modules generated by mechanical load tests. Solar Energy Materials and Solar Cells. 2011, 95(11): 3054–3059. doi: 10.1016/j.solmat.2011.06.032

[3] Luo B, Gallas S, Micallef C, et al. Experimental and finite element modal analysis of photovoltaic modules for the design of next-generation vehicle-integrated PV applications. Solar Energy Materials and Solar Cells. 2025, 290: 113683. doi: 10.1016/j.solmat.2025.113683

[4] Bergmann S, Hassani F, Javanbakht Z, Aßmus M. On a fast analytical approximation of natural frequencies for photovoltaic modules. Technische Mechanik—European Journal of Engineering Mechanics. 2020, 40(2): 191–203. doi: 10.24352/UB.OVGU-2020-025

[5] Lindroos J, Fenning DP, Backlund DJ, et al. Nickel: A very fast diffuser in silicon. Journal of Applied Physics. 2013, 113(20): 204906. doi: 10.1063/1.4807799

[6] Abdurakhmanov BA, Bakhadirkhanov MK, Ayupov KS, et al. Formation of clusters of impurity atoms of nickel in silicon and controlling their parameters. Nanoscience and Nanotechnology. 2014, 4(2): 23–26. doi: 10.5923/j.nn.20140402.01

[7] Bakhadyrkhanov MK, Valiev SA, Zikrillaev NF, et al. Silicon photovoltaic cells with clusters of nickel atoms. Applied Solar Energy. 2016, 52(4): 278–281. doi: 10.3103/S0003701X1604006X

[8] Bakhadyrkhanov MK, Kenzhaev ZT. Optimal conditions for nickel doping to improve the efficiency of silicon photoelectric cells. Technical Physics. 2021, 66(7): 851–856. doi: 10.1134/S1063784221060049

[9] Kenzhaev ZT, Iliev HM, Ismailov KA, et al. Physical mechanisms of gettering properties of nickel clusters in silicon solar

cells. Physical Sciences and Technology. 2024, 11(1–2): 13–22. doi: 10.26577/phst2024v11i1a2

[10] Leissa AW. Vibration of Plates. NASA SP-160. National Aeronautics and Space Administration; 1969.

[11] Hopcroft MA, Nix WD, Kenny TW. What is the Young's modulus of silicon? Journal of Microelectromechanical Systems. 2010, 19(2): 229–238. doi: 10.1109/JMEMS.2009.2039697

[12] Ledbetter HM, Reed RP. Elastic properties of metals and alloys, I: Iron, nickel, and iron-nickel alloys. Journal of Physical and Chemical Reference Data. 1973, 2(3): 531–617. doi: 10.1063/1.3253127

[13] Huang M, Yang C, Cai K, et al. Modal analysis of flexible photovoltaic support system using multi-source data. Journal of Civil Structural Health Monitoring. 2025, 15: 3321–3343. doi: 10.1007/s13349-025-00992-0

[14] Castellini P, Martarelli M, Tomasini EP. Laser Doppler vibrometry: Development of advanced solutions answering to technology's needs. Mechanical Systems and Signal Processing. 2006, 20(6): 1265-1285. doi: 10.1016/j.ymssp.2005.11.015

[15] Mindlin RD. Influence of rotatory inertia and shear on flexural motions of isotropic, elastic plates. Journal of Applied Mechanics. 1951, 18(1): 31-38. doi: 10.1115/1.4010217